

LETTER TO THE EDITOR

Discovery of a hot post-AGB star in Galactic globular cluster E3

R. Kumar^{1,2}, A. Moharana³, S. Piridi², A. C. Pradhan², K.G. Hełminiak³, N. Ikonnikova⁴, A. Dodin⁴, R. Szczerba^{5,3}, M. Giersz⁶, D. K. Ojha⁷, and M. R. Samal¹

¹ Astronomy and Astrophysics Division, Physical Research Laboratory, Navrangpura, Ahmedabad - 380009, Gujarat, India

e-mail: ranjankmr488@gmail.com, acp.phy@gmail.com

² Department of Physics and Astronomy, National Institute of Technology, Rourkela - 769008, Odisha, India

³ Nicolaus Copernicus Astronomical Center, Polish Academy of Sciences, ul. Rabiańska 8, 87-100 Toruń, Poland

⁴ Sternberg Astronomical Institute of the Lomonosov Moscow State University, University av. 13, 119234 Moscow, Russia

⁵ Xinjiang Astronomical Observatory, Chinese Academy of Sciences 150 Science 1-Street, Urumqi, Xinjiang 830011, China

⁶ Nicolaus Copernicus Astronomical Centre, Polish Academy of Sciences, ul. Bartycka 18, 00-716 Warsaw, Poland

⁷ Department of Astronomy and Astrophysics, Tata Institute of Fundamental Research, Mumbai - 400005, India

Received: 28 February 2024 / Accepted: 20 April 2024

ABSTRACT

We report a new hot post-asymptotic giant branch (PAGB) star in the Galactic globular cluster (GC) E3, which is one of the first of the identified PAGB stars in a GC to show a binary signature. The star stands out as the brightest source in E3 in the *Astrosat*/UVIT images. We confirmed its membership with the cluster E3 using Gaia DR3 kinematics and parallax measurements. We supplemented the photometric observations with radial velocities (RVs) from high-resolution spectroscopic observations at two epochs and with ground- and space-based photometric observations from 0.13 μm to 22 μm . We find that the RVs vary over $\sim 6 \text{ km s}^{-1}$ between the two epochs. This is an indication of the star being in a binary orbit. A simulation of possible binary systems with the observed RVs suggests a binary period of either 39.12 days or 17.83 days with mass ratio $q \geq 1.0$. The $[\text{Fe}/\text{H}]$ derived using the high-resolution spectra is ~ -0.7 dex, which closely matches the cluster metallicity. The spectroscopic and photometric measurements suggest T_{eff} and $\log g$ of the star as $17500 \pm 1000 \text{ K}$ and 2.37 ± 0.20 dex, respectively. Various PAGB evolutionary tracks on the Hertzsprung–Russell (H–R) diagram suggest a current mass of the star in the range 0.51–0.55 M_{\odot} . The star is enriched with C and O abundances, showing similar CNO abundances compared to the other PAGB stars in GCs with the evidence of the third dredge-up on the AGB phase.

Key words. Stars: AGB and post-AGB – (Galaxy:) globular clusters: individual: E3

1. Introduction

Post-asymptotic giant branch (PAGB) stars are the most luminous objects in globular clusters (GCs). They evolve from the top of the AGB and move leftward in the HR diagram at almost constant luminosity (Kwok 1982, 1993). They are rare in GCs (one or two per cluster is expected) due to the fact that PAGB stars have a very short lifetime (≤ 0.5 Myr; Moehler et al. 2019) compared to the age of GCs (10–12 Gyr; Harris 1996). Nevertheless, a handful of PAGB stars have been detected in more than 150 Galactic GCs (for details, see Moehler et al. 2019; Davis et al. 2022; Dixon 2024).

There are three major categories of PAGB stars observed in GCs based upon the evolution of their progenitors on the horizontal branch (HB), the core He burning phase. The first category is for HB stars with H-rich envelopes, which ascend towards the AGB; they have several thermal pulses at the tip of the AGB. Their post-AGB phase is treated as the normal PAGB phase (Greggio & Renzini 1990; Dorman et al. 1993; Moehler et al. 2019). The second category is for HB stars with H-poor envelopes but

H-envelopes $> 0.02 M_{\odot}$, which ascend towards the AGB, but never reach the AGB tip and leave the AGB phase early¹ (Moehler et al. 2019). Their PAGB phase is known as post-early-AGB (PEAGB) phase (Greggio & Renzini 1990; Dorman et al. 1993; Moehler et al. 2019). They are less luminous than the normal PAGB stars (Dorman et al. 1993; Moehler et al. 2019). The third category of PAGB stars is for stars that evolved from HB stars with H-envelopes $< 0.02 M_{\odot}$ (extreme-HB stars) (Dorman et al. 1993; Moehler et al. 2019). They never reach the AGB phase; rather, they remain hot and luminous during their post-HB evolution, and ultimately cool down through the white dwarf (WD) phase. These PAGB stars are known as AGB-manqué stars (Dorman et al. 1993; Gratton et al. 2010; Moehler et al. 2019).

In a cluster with a large binary fraction, a few red-giant-branch (RGB) stars in a binary system lose enough mass to their companion. They become inefficient in igniting He during the RGB phase and evolve off the RGB at the lumi-

¹ Either having one or two thermal pulses or without experiencing any thermal pulse.

nosity comparable to their RGB tip. These stars are called post-RGB stars (Lei et al. 2015; Kamath et al. 2016). They have similar luminosities to PEAGB stars and ignite He either on their post-RGB phase or the WD cooling track (Cassisi et al. 2003; Miller Bertolami et al. 2008; Lei et al. 2015).

Moehler et al. (2019) performed a comprehensive analysis of 78 Galactic GCs to identify the hot PAGB stars. They found 19 new PAGB stars in addition to 12 previously known PAGB/PEAGB stars. Prabhu et al. (2021) have detected five PAGB stars in the NGC 2808 using ultraviolet (UV) images of Ultraviolet Imaging Telescope (UVIT) on board *AstroSat* (Tandon et al. 2017). Davis et al. (2022) studied 97 Galactic GCs using optical filters and found 13 cooler (F and G type) PAGB stars among them. Dixon (2024) studied the CNO and s-process abundances of 17 previously known PAGB stars in the Galactic GCs to find evidence of the third dredge-up (3DU) among GC PAGB stars. Considering all the above surveys, a total of 42 unique PAGB/PEAGB/AGB-manqué stars have been observed so far only in ~ 20 GCs when exploring more than 150 Galactic GCs. None of them has shown a binary signature (neither photometric nor spectroscopic). However, the low-mass PAGB stars, V29 in ω cen and K648 in M15, indicate that they have evolved in a binary system (Dixon 2024).

In this paper we report the discovery of a new hot PAGB star in Galactic GC E3 (ESO 37-1; Lauberts 1976) using UV images from UVIT and Gaia DR3 data. Cluster E3 (RAJ2000=09:20:57.07, DEJ2000=-77:16:54.8; Harris 1996, 2010) is one of the faintest GCs in the Milky Way, and is likely to be the least massive one ($2.9 \times 10^3 M_{\odot}$; Sollima & Baumgardt 2017). It is a metal-rich cluster ($[Fe/H] \sim -0.7$ dex; de la Fuente Marcos et al. 2015; Salinas & Strader 2015; Monaco et al. 2018) with a moderate reddening ($E(B - V) = 0.29$; Schlafly & Finkbeiner 2011). The cluster has the largest binary fraction (72%) among Galactic GCs (Milone et al. 2012).

2. Photometric and spectroscopic observations

Cluster E3 was observed in two far-UV (FUV: 1300–1800 Å) filters, F154W and F169M, of UVIT. The total exposure times of the F169M and F154W filters are 6047 sec and 3546 sec, respectively. The field of view (FoV) of UVIT is sufficient to cover the entire cluster (tidal radius = 8.49 arcmin, Harris 1996). However, we see only two FUV bright sources within the FoV of UVIT; one is within the half-light radius of the cluster, and the other is at the edge of the image (Fig. 1). The sources at the edges of the UVIT FoV are unreliable due to edge artefacts; hence, they were excluded during photometry. Finally, we detected eight sources in the FUV (red circles in Fig. 1).

We used the GC catalogue of Gaia DR3 (GCG21; Vasiliev & Baumgardt 2021) for cluster membership analysis (see details of the analysis in Appendix A). We found only one out of eight UVIT observed sources to be a cluster member, which is indicated by the red arrow in Fig. 1. The source is bright in FUV and optical bands (Table 1) and lies well within the half-light radius of the cluster. In Fig. 2 we show all the Gaia observed cluster member sources (grey dots) and the UVIT observed cluster member source (blue asterisk) on the vector-point diagram (left panel) and the parallax versus PMRA (middle upper panel) and parallax versus PMDEC (middle lower panel). We find that

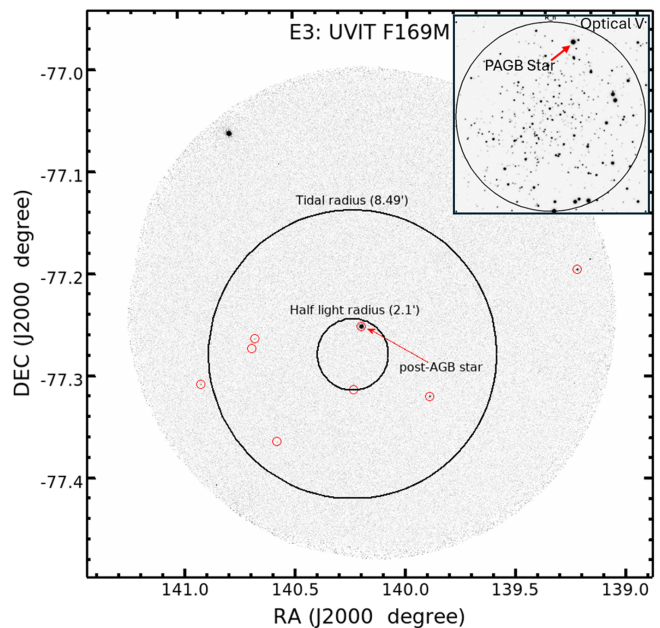


Fig. 1. UVIT F169M filter image of E3. The half-light and tidal radius of E3 ($R_h = 2.1'$ and $R_t = 8.49'$, Harris 1996, 2010) are well within the field of view of UVIT. The red arrow indicates the probable post-AGB star. In the inset (upper right corner) the optical V-band image (Stetson et al. 2019) of the cluster (up to half-light radius) is shown. The PAGB star is easily distinguishable as one of the cluster's brightest stars in both images.

the proper motion and the parallax values of the UVIT observed source are in good agreement with the Gaia observed cluster member sources (Fig. 2). The Gaia BP–RP versus G colour-magnitude diagram (CMD) (right panel of Fig. 2) suggests that the source is an evolved PAGB star in the GC E3.

2.1. Spectroscopic observations of the PAGB star

The spectroscopic observations of the PAGB star were obtained at two epochs (17 February 2023 and 26 March 2023) with a high-resolution ($R \sim 28\,000$) CHIRON² spectrograph (Tokovinin et al. 2013) installed on the SMARTS 1.5 m telescope at the CTIO observatory, Chile. The observation details are given in Table B.1, and the reduction procedure of the spectra is explained in Appendix B.

2.1.1. Radial velocities

We measured the radial velocities (RVs) using our own implementation (Helminiak et al. 2019) of the TODCOR technique (Zucker & Mazeh 1994). The procedure is described in Appendix C. The barycentric RVs were estimated as 40.20 ± 0.57 km s⁻¹ and 34.66 ± 0.85 km s⁻¹ for the spectra observed at the first and second epochs, respectively. These values are quite high with respect to the mean RV of the cluster (12.6 km s⁻¹; Monaco et al. 2018). However, the change in velocities between two epochs is quite substantial; this signals the possible binarity of the star. Since the cluster has a large binary fraction (Milone et al. 2012), it is possible that the identified PAGB star is evolving in a binary system. In Appendix D we present the performed

² <http://www.astro.yale.edu/smarts/1.5m.html>

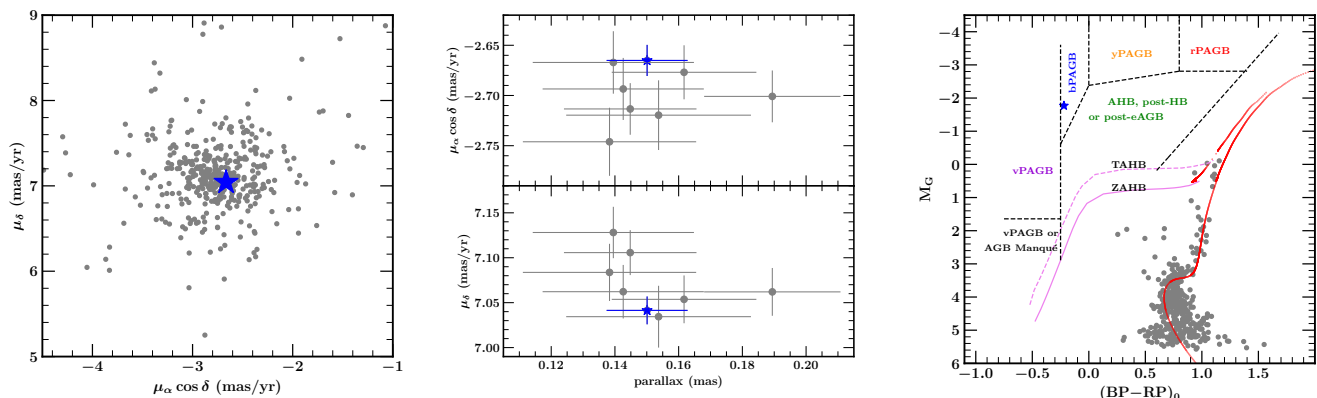


Fig. 2. Diagrams showing the kinematics and photometric analysis of the cluster member sources with the Gaia data. The left panel shows the vector-point diagram of the cluster member sources from the Gaia catalogue (Vasiliev & Baumgardt 2021, grey dots) and the UVIT observed cluster member source (blue asterisk). The middle panel shows the parallax vs proper motion in RA (top) and DEC (bottom) for the Gaia-observed cluster members having parallax S/N (plx/e_plx) > 5 (grey dots) and the UVIT observed cluster member source (blue asterisks). The right panel shows BP–RP versus M_G CMD in the absolute magnitude plane. The Gaia G magnitudes (grey dots) are scaled to absolute magnitudes using distance modulus, $m-M = 14.50$ (Baumgardt & Vasiliev 2021). The BaSTI-IAC isochrone of age 11 Gyr, $[Fe/H] = -0.70$ dex is overplotted as a red solid line. The zero-age HB (ZAHB) and terminal-age HB (TAHB) loci are shown as solid pink and dashed lines, respectively. The black dashed line shows different subcategories of PAGB and post-HB stars, as defined in Bond (2021).

Table 1. Observation details of the PAGB star.

RA (J2000) (hh:mm:ss.ss)	DEC (J2000) (dd:mm:ss.ss)	Parallax (mas)	PMRA (mas/yr)	PMDEC (mas/yr)	Gaia/G	UVIT/F154W	UVIT/F169M	Gaia ID
09:20:48.02	-77:15:15.36	0.1501 ± 0.0127	-2.6651 ± 0.0155	7.0414 ± 0.0155	13.576	14.700	14.670	5203319520096719360

simulations for possible binary configurations of the PAGB star with constraints from the RVs. The simulations create binary models with different primary mass values in the range 0.2–0.8 M_\odot . We find the period of the binary models is spread around 39.12 days (51% of the models) and 17.83 days (16.4% of the models) (Fig. D.1). This suggests a close orbit of the system. The mass ratio³ (q) of the system lies in the range of 0.2–1.5. Milone et al. (2012) calculated photometric binary fractions for E3 and found that around 40% of the cluster members have a binary with $q > 0.5$. We do not see another companion in the spectra, so $q > 1.5$ (a conservative upper limit) is unlikely. Since the source is close to the half-light radius, it is likely to have a heavier companion. Hence, we suggest $q \geq 1.0$ for the binary system. However, further spectroscopic monitoring is required to confirm the binarity and characterise the companion.

2.1.2. Atmospheric parameters and abundances

The atmospheric parameters (T_{eff} and $\log g$) of the PAGB star were derived from CHIRON spectra using a relation involving the ionisation balance between Si II and Si III, for a set of T_{eff} and $\log g$ pairs from TLUSTY model grid BSTAR2006 (Lanz & Hubeny 2007). The procedure of atmospheric parameter estimation is described in Appendix E. We find $T_{\text{eff}} = 17000^{+400}_{-700}$ K, $\log g = 2.37 \pm 0.20$, and $\log \epsilon_{\text{Si}} = 7.31 \pm 0.05$ from the spectral analysis of the PAGB star.

Using the above parameters derived from the spectra of the PAGB star, we derived abundances (ϵ) of all elements detected in the spectrum. The chemical composition

analysis of the individual elements is given in Appendix F, and the abundance value of each element is given in Table F.1. The derived individual abundances of metals in the star are two to five times lower than in the Sun (Table F.1), suggesting that the star is metal poor. The $[Fe/H]$ abundance (-0.7 ± 0.2 dex) matches the cluster metallicity (Monaco et al. 2018). Unlike this star, many PAGB binaries show depletion of iron (van Winckel 2003). However, in a recent study to understand depletion in binary RV Tauri stars (and a few binary PAGB stars), Gezer et al. (2015) found that iron depletion is prevalent in binaries with an accretion disk or with evidence of a former disk. The binaries without a disk do not show any depletion. Since we do not find any signature of an accretion disk (or depletion), the identified PAGB star might be a case where the evolution in a binary does not involve the formation of an accretion disk.

2.2. Spectral energy distribution of the PAGB star

We performed the spectral energy distribution (SED) fitting of the PAGB star in the VO SED analyzer (VOSA; Bayo et al. 2008). The SED fitting procedure is described in Appendix G. We found that the best-fitting model grid has $T_{\text{eff}} = 18000$ K and $\log g = 2.25$. The best-fitting model and observed fluxes are shown in Fig. G.1. VOSA also provides the bolometric luminosity (L_{bol}) and radius of the star (R) from their best-fit stellar atmosphere model grid based on the distance of the star and the total observed fluxes from the UV to IR bands. We found L_{bol} and R of the identified PAGB star as $2136 \pm 150 L_\odot$ ($\log(L/L_\odot) = 3.33 \pm 0.03$) and $4.61 \pm 0.14 R_\odot$, respectively.

³ The ratio of the companion mass to the PAGB mass.

3. Evolutionary status of the PAGB star

In Fig. 3 we show all the previously observed PAGB stars (blue asterisks) in GCs with known T_{eff} , L_{bol} , and $\log g$ values. The newly identified PAGB star in this paper is shown as a red asterisk. We find that the luminosity of the identified PAGB star is similar to most of the GC PAGB stars ($\log(L/L_{\odot}) \sim 3.25$; Dixon 2024). We show all the latest available PAGB evolutionary tracks with H-burning (upper left panel) and He-burning (lower left panel) prescriptions. The H-burning evolutionary tracks of initial masses 0.9, 1.0, and 1.25 M_{\odot} (dashed red, black, and green lines, respectively) are from Miller Bertolami (2016). The PAGB evolutionary tracks of Moehler et al. (2019) (solid lines) were generated from an initial mass of 0.85 M_{\odot} , but they differ in their post-HB evolution based upon their location and mass on the HB phase. We find that the luminosity of evolutionary tracks varies upon their initial and/or final mass. The current mass of the identified PAGB star would be $\sim 0.51 M_{\odot}$ based upon the H-burning evolutionary tracks (upper left panel of Fig. 3).

The derived $\log g$ value of the star is lower than the other PAGB stars observed in Galactic GCs (right panel of Fig. 3). The evolutionary tracks on the $\log g$ versus $\log T_{\text{eff}}$ plane suggest that the current mass of the identified PAGB star is $\sim 0.55 M_{\odot}$, which evolved from an initial mass of 1.0 M_{\odot} (Miller Bertolami 2016).

Hence, various evolutionary tracks on the T_{eff} , L_{bol} , and $\log g$ plane suggest a current mass of the PAGB star in the range 0.51 – 0.55 M_{\odot} which has spent ~ 1000 yr in the PAGB phase (1.0 M_{\odot} track; Miller Bertolami 2016). This mass range of the PAGB star indicates that the companion is also an evolved post-main sequence (of 0.5 – 0.8 M_{\odot} for $q \geq 1.0$). The very close orbit of the system suggests that it would have gone into a common-envelope interaction that drastically shortened the orbital period (and ejected material into the ISM). In this case, the evolution of the star would have been interrupted compared to that of a single star. However, the star shows higher luminosity than would have resulted from interrupted evolution (black dotted line in the lower panel of Fig. 3, left panel), but a lower luminosity than would have resulted from a single star evolution (dashed lines in the upper panel of Fig. 3, left panel).

Recently, Davis et al. (2022) showed that PAGB stars are preferentially found in metal-poor clusters with blue or very blue HB stars. On the other hand, the identified PAGB star is in E3, a relatively metal-rich cluster containing red HB stars, which is one of the few cases of metal-rich clusters that contain PAGB stars (such as the famous blue star in 47 Tucanae). However, since the PAGB in E3 has a similar luminosity to the PAGB stars in metal-poor GCs, a binary configuration better supports its presence in a metal-rich and red HB cluster.

4. Evidence of third dredge-up in the PAGB star

PAGB stars, which undergo thermal pulses at the AGB-tip, bring up the processed materials to the surface (3DU process); as a result, the enhanced C, O, and other s-process elements could be found on the surface of PAGB stars. Recently, Dixon (2024) studied the CNO abundances of 11 PAGB stars observed in the Galactic GCs and found 4 of them have enhanced CNO abundances compared to the CNO abundance of their respective host cluster. They con-

cluded that the increased C and O abundances during their 3DU enhanced the overall CNO abundance in those PAGB stars.

In Fig. 4 we plot the abundance ratios of C/CNO versus C (left panel) and N/O versus O (right panel) abundances of the eight PAGB stars for which C abundances were reported in Dixon (2024) (blue asterisks for the PAGB stars having 3DU and black asterisks for those having no sign of 3DU) along with the abundances of the identified PAGB star in this paper (red asterisk). We find that the identified PAGB star has similar C and O abundances to those PAGB stars of other GCs that have undergone the 3DU. This suggests the discovered PAGB star also went to the 3DU while on its AGB evolution.

5. Conclusion

We explore all the photometric and spectroscopic details of the new hot PAGB star discovered in GC E3. The proper motion and parallax of the star from Gaia DR3 support its membership, and the location of the star in the absolute CMD suggests that the star is in the PAGB phase. The radial velocities show a variation of $\sim 6 \text{ km s}^{-1}$ between the two epochs, suggesting a binary nature of the star. A simulation of possible binary systems with the observed RV values of the PAGB star and the cluster mean RV suggest that the binary period of the star is around 39 days (51% of models) or 18 days (16% of models). The abundances were derived for the He, C, N, O, Ne, Al, Si, S, and Fe lines. The metallicity of the star ($[\text{Fe}/\text{H}] = -0.7$ dex) agrees with the cluster metallicity. We find the T_{eff} , $\log g$, $\log L$, and radius of the PAGB star to be $17500 \pm 1000 \text{ K}$, 2.37 ± 0.20 , 3.33 ± 0.03 , and $4.61 \pm 0.14 R_{\odot}$, respectively, using SED fitting of 30 photometric fluxes from UV to IR bands. A comparison of various PAGB evolutionary tracks with the observed star on the H-R diagram suggests that the current mass of the PAGB star is in the range 0.51–0.55 M_{\odot} . A comparison of the observed C, N, and O abundances of the star with the abundances of the PAGB stars of other GCs that show 3DU suggest that the PAGB star has undergone the 3DU and enriched its C and O abundances. Future multi-epoch spectroscopic observations are necessary to constrain the period and better understand the binary nature of the identified hot PAGB star.

Acknowledgements. We thank the referee for his/her constructive comments. We thank Prof. M. Parthasarathy for his valuable discussion during the initial phase of the project. The CHRION spectra were obtained with the help of the National Science Center (NCN), Poland, using grant no. 2021/41/N/ST9/02746. AM is also supported by this NCN grant. ACP and SP acknowledge the support of the Indian Space Research Organisation (ISRO) under the AstroSat archival Data utilization program (No. DS_2B-13013(2)/1/2022-Sec.2). MG was partially supported by the NCN through the grant UMO-2021/41/B/ST9/01191. DKO acknowledges the support of the Department of Atomic Energy, Government of India, under Project Identification No. RTI 4002. The research work at the Physical Research Laboratory is funded by the Department of Space, Government of India. This publication uses the data from the *AstroSat* mission of the ISRO, archived at the Indian Space Science Data Center (ISSDC).

References

- Asplund, M., Grevesse, N., Sauval, A. J., & Scott, P. 2009, *ARA&A*, 47, 481
 Baumgardt, H. & Vasiliev, E. 2021, *MNRAS*, 505, 5957

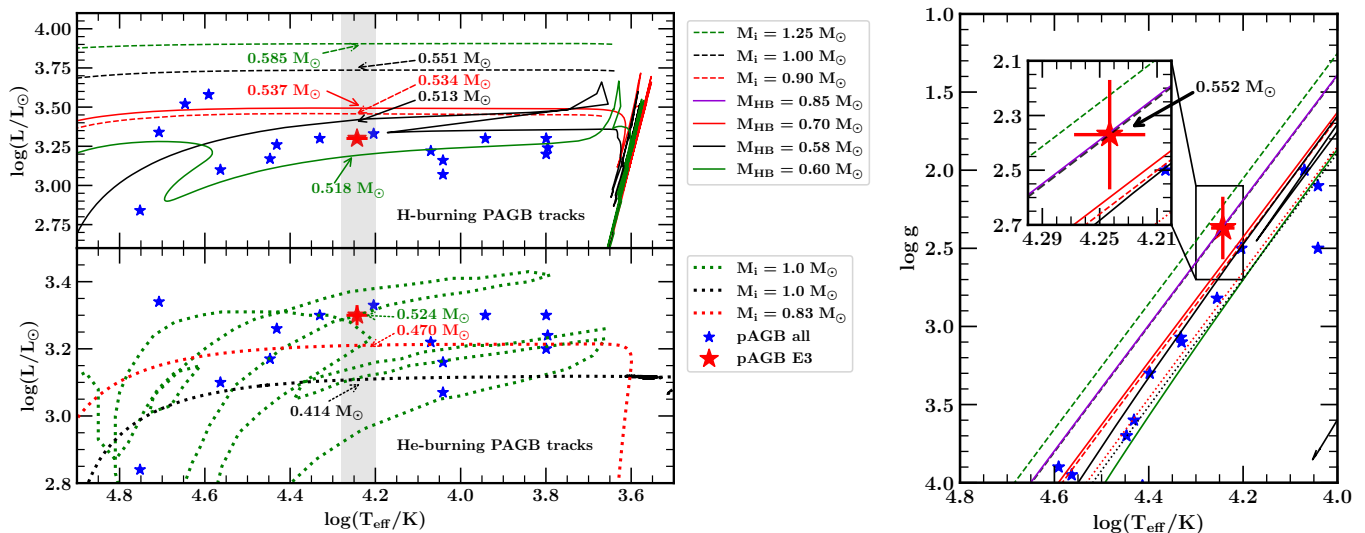


Fig. 3. The $\log T_{\text{eff}}$ versus $\log L$ (left panel) and $\log T_{\text{eff}}$ versus $\log g$ (right panel) plots display PAGB stars that have been observed in GCs. The red asterisk indicates the newly discovered PAGB star in E3, and the blue asterisks indicate PAGB stars found in other GCs. In the upper left panel, the H-burning PAGB evolutionary tracks of Miller Bertolami (2016) and Moehler et al. (2019) with metallicity $Z = 0.001$ are shown as dashed and solid lines, respectively, and for different initial and HB masses (as shown in the legend at right). The PAGB tracks of Moehler et al. (2019) consider an initial mass of $0.85 M_{\odot}$ for all the evolutionary tracks. The lower left panel shows the post-RGB He-burning evolutionary tracks from Bloeker (1995) (green dotted line), Lei et al. (2015) (red dotted line), and Driebe et al. (1998) (black dotted line). The grey shaded region indicates a T_{eff} range of 16 000 – 19 000 K. The current mass for each evolutionary track at $\sim 18 000$ K is shown with an arrow of the same colour and style as the evolutionary track. In the right panel, PAGB stars are shown on the $\log T_{\text{eff}}$ versus $\log g$ plane. The inset shows the zoomed-in view around the newly identified PAGB star.

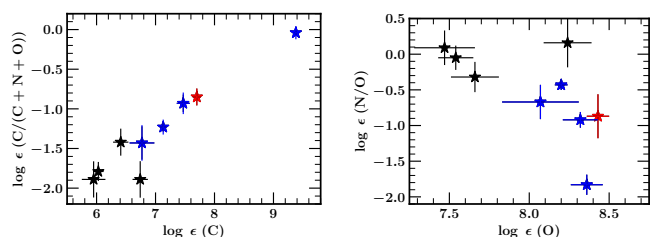


Fig. 4. Comparison between abundance ratios of PAGB star of E3 and other GCs. PAGB stars with 3DU evidence are shown as blue asterisks; those with no 3DU evidence are shown as black asterisks. The newly identified PAGB star of E3 is shown as a red asterisk. The left panel shows C/CNO versus C abundance plot, whereas the right panel shows N/O vs O abundance plot.

Bayo, A., Rodrigo, C., Barrado Y Navascués, D., et al. 2008, *A&A*, 492, 277
Bloeker, T. 1995, *A&A*, 299, 755
Bond, H. E. 2021, *AJ*, 161, 204
Cardelli, J. A., Clayton, G. C., & Mathis, J. S. 1989, *ApJ*, 345, 245
Cassisi, S., Schlattl, H., Salaris, M., & Weiss, A. 2003, *ApJ*, 582, L43
Conroy, K. E., Kochoska, A., Hey, D., et al. 2020, *ApJS*, 250, 34
Cutri, R. M., Wright, E. L., Conrow, T., et al. 2021, *VizieR Online Data Catalog*, II/328
Davis, B. D., Bond, H. E., Siegel, M. H., & Ciardullo, R. 2022, *ApJ*, 926, 99
de la Fuente Marcos, R., de la Fuente Marcos, C., Moni Bidin, C., Ortolani, S., & Carraro, G. 2015, *A&A*, 581, A13
Denis, C. 2005, *VizieR Online Data Catalog*, B/denis
Dixon, W. V. 2024, *ApJ*, 961, 24
Dorman, B., Rood, R. T., & O’Connell, R. W. 1993, *ApJ*, 419, 596
Driebe, T., Schoenberner, D., Bloeker, T., & Herwig, F. 1998, *A&A*, 339, 123
Gezer, I., Van Winckel, H., Bozkurt, Z., et al. 2015, *MNRAS*, 453, 133

Gratton, R. G., D’Orazi, V., Bragaglia, A., Carretta, E., & Lucatello, S. 2010, *A&A*, 522, A77
Greggio, L. & Renzini, A. 1990, *ApJ*, 364, 35
Harris, W. E. 1996, *AJ*, 112, 1487
Harris, W. E. 2010, arXiv e-prints, arXiv:1012.3224
Helminiak, K. G., Konacki, M., Różycka, M., et al. 2012, *MNRAS*, 425, 1245
Helminiak, K. G., Tokovinin, A., Niemczura, E., et al. 2019, *A&A*, 622, A114
Henden, A. A., Levine, S., Terrell, D., & Welch, D. L. 2015, in *American Astronomical Society Meeting Abstracts*, Vol. 225, American Astronomical Society Meeting Abstracts #225, 336.16
Hubeny, I., Allende Prieto, C., Osorio, Y., & Lanz, T. 2021, arXiv e-prints, arXiv:2104.02829
Hubeny, I. & Lanz, T. 1995, *ApJ*, 439, 875
Kamath, D., Wood, P. R., Van Winckel, H., & Nie, J. D. 2016, *A&A*, 586, L5
Kwok, S. 1982, *ApJ*, 258, 280
Kwok, S. 1993, *ARA&A*, 31, 63
Lanz, T. & Hubeny, I. 2007, *ApJS*, 169, 83
Lauberts, A. 1976, *A&A*, 52, 309
Lei, Z., Chen, X., Zhang, F., & Han, Z. 2015, *MNRAS*, 449, 2741
Leinert, Ch., Bowyer, S., Haikala, L. K., et al. 1998, *Astron. Astrophys. Suppl. Ser.*, 127, 1
Lindegren, L., Bastian, U., Biermann, M., et al. 2021, *A&A*, 649, A4
Mello, D. R. C., Dafon, S., Pereira, C. B., & Hubeny, I. 2012, *A&A*, 543, A11
Miller Bertolami, M. M. 2016, *A&A*, 588, A25
Miller Bertolami, M. M., Althaus, L. G., Unglaub, K., & Weiss, A. 2008, *A&A*, 491, 253
Milone, A. P., Piotto, G., Bedin, L. R., et al. 2012, *A&A*, 540, A16
Moehler, S., Landsman, W. B., Lanz, T., & Miller Bertolami, M. M. 2019, *A&A*, 627, A34
Moharana, A., Helminiak, K. G., Marcadon, F., et al. 2023, *MNRAS*, 521, 1908
Monaco, L., Villanova, S., Carraro, G., Mucciarelli, A., & Moni Bidin, C. 2018, *A&A*, 616, A181
Nelder, J. A. & Mead, R. 1965, *The Computer Journal*, 7, 308
Prabhu, D. S., Subramaniam, A., & Sahu, S. 2021, *ApJ*, 908, 66

- Rucinski, S. 1999, in *Astronomical Society of the Pacific Conference Series*, Vol. 185, IAU Colloq. 170: Precise Stellar Radial Velocities, ed. J. B. Hearnshaw & C. D. Scarfe, 82
- Salinas, R. & Strader, J. 2015, *ApJ*, 809, 169
- Schiavon, R. P., Dalessandro, E., Sohn, S. T., et al. 2012, *AJ*, 143, 121
- Schlafly, E. F. & Finkbeiner, D. P. 2011, *ApJ*, 737, 103
- Skrutskie, M. F., Cutri, R. M., Stiening, R., et al. 2006, *AJ*, 131, 1163
- Sollima, A. & Baumgardt, H. 2017, *MNRAS*, 471, 3668
- Stetson, P. B., Pancino, E., Zocchi, A., Sanna, N., & Monelli, M. 2019, *MNRAS*, 485, 3042
- Tandon, S. N., Subramaniam, A., Girish, V., et al. 2017, *AJ*, 154, 128
- Tokovinin, A., Fischer, D. A., Bonati, M., et al. 2013, *PASP*, 125, 1336
- van Winckel, H. 2003, *ARA&A*, 41, 391
- Vasiliev, E. & Baumgardt, H. 2021, *MNRAS*, 505, 5978
- Zinn, R. J., Newell, E. B., & Gibson, J. B. 1972, *A&A*, 18, 390
- Zucker, S. & Mazeh, T. 1994, *ApJ*, 420, 806

Appendix A: Cluster membership analysis using Gaia DR3

The GC catalogue of Gaia EDR3 (GCG21; Vasiliev & Baumgardt 2021) provides information about the source positions (RA, DEC), proper motions (PMRA, PMDEC), parallax,⁴ cluster membership probability, and photometric magnitudes in G, BP, and RP filters for sources observed in the 170 Galactic GCs. We found 479 Gaia observed sources of E3 within the UVIT FoV having cluster membership probability > 90%. We cross-matched the eight UVIT observed sources with the Gaia catalogue and found only one source to be a cluster member. The UVIT observed cluster member source has a membership probability of 99% and lies well within the half-light radius of the cluster. For parallax information, we selected only those cluster member sources with good parallax ($S/N > 5$) and found only 8 out of 479 cluster member sources. The mean proper motions and parallax of the cluster estimated by Vasiliev & Baumgardt (2021) are PMRA ($\mu_{\alpha}\cos\delta$) = -2.727 ± 0.027 (mas/yr), PMDEC (μ_{δ}) = 7.083 ± 0.027 (mas/yr), and parallax ($\bar{\omega}$) = 0.146 ± 0.013 , respectively. We find that the proper motion and the parallax values of the UVIT observed cluster member source are in good agreement with the Gaia observed cluster member sources (Fig. 2). The details of the UVIT and the Gaia observations of the source are given in Table 1.

In the right panel of Fig. 2, we show the optical CMD of the cluster member sources (grey dots) in the absolute magnitude plane. The colours and magnitudes of the Gaia filters are dereddened using $E(B-V) = 0.29$ (Schlafly & Finkbeiner 2011) and the Cardelli et al. (1989) extinction law. The Gaia G magnitudes are scaled to the absolute magnitudes using the distance modulus, $m-M = 14.50$ (Baumgardt & Vasiliev 2021). The UVIT observed source (blue asterisk) is ~ 2.0 mag brighter than the other cluster member sources and appears bluer in colour ($BP-RP = -0.2$ mag), which is the location of the blue evolved stars of GCs (Zinn et al. 1972; Moehler et al. 2019; Bond 2021). We marked various regions of PAGB stars, defined by Bond (2021) as red-PAGB (rPAGB), yellow-PAGB (yPAGB), blue-PAGB (bPAGB), and AGB-manqué stars, on the Gaia BP-RP versus G CMD (right panel of Fig. 2). The UVIT observed cluster member source can be found in the bPAGB region. Hence, we confirm that the source is an evolved PAGB star and a bona fide member of the GC E3.

Appendix B: Reduction of CHIRON spectra of the PAGB star

We reduced the spectra with the pipeline developed at Yale University (Tokovinin et al. 2013). Wavelength calibrations were performed using the ThAr lamp exposures taken during the scheduled calibration runs. We applied barycentric corrections separately using calculations from IRAF with the *bvcor* task. We calculated the signal-to-noise ratio (S/N) of the two spectra using the *snr*⁵ module in SPECUTILS. We found a S/N of 40.6 and 25.6 for the spectra at the first and second epochs, respectively.

⁴ The catalogue provides zero point corrected parallax values, as suggested by Lindegren et al. (2021).

⁵ <https://specutils.readthedocs.io/en/stable/analysis.html>

Table B.1. Details of the spectroscopic observations of the PAGB star.

Epoch	Date of Observation	Exposure Time	S/N
1	17 February 2023	4×1600 sec.	40.6
2	26 March 2023	4×1600 sec.	25.6

The optical spectrum of the star in the spectral ranges 4505–6602 Å shows about 50 stellar absorption lines. The identification of the lines is based on the National Institute of Standards and Technology (NIST) Atomic Spectra Database.⁶

Absorption lines of neutral species including H I ($H\alpha$ and $H\beta$), He I, C I, N I, O I, and Ne I were identified. Singly ionised species including C II, N II, O II, Si II, S II, Mg II, and Fe II were detected. Higher ionisation is seen in Al III, Fe III, Si III, and S III.

The spectrum of the star also contains absorption features that have interstellar origin. There is a Na I doublet ($\lambda 5889.951, 5895.924$) and several very weak diffuse interstellar bands (DIBs). Emission lines are not detected in the spectrum of the star, in contrast to many hot post-AGB stars, whose spectra consist of two components: the star's absorption spectrum and an overlain emission spectrum from a low-excitation gas envelope (Mello et al. 2012). Comparing the spectra at the two epochs, we find static O I emission lines at 5577 Å, 6300 Å, and 6364 Å, which are most probably due to air-glow (Leinert, Ch. et al. 1998), and therefore we did not consider them for our analysis. The complete continuum-normalised spectrum of the star in the spectral ranges 4505–6602 Å is presented at http://lfnm1.sai.msu.ru/~davnv/E3/atlas_E3.pdf.

Appendix C: RV estimation from the spectra of the PAGB star

The RVs were measured on prominent absorption lines, including He lines, but avoiding $H\alpha$ and $H\beta$ as they had broad absorption lines (FWHM > 100 km s⁻¹) affecting a precise RV estimate. We used a template with $T_{\text{eff}} = 20000$ K, $\log g = 4.5$ dex, and solar metallicity to create the cross-correlation functions (CCF; Fig. C.1) using the TODCOR technique (Zucker & Mazeh 1994). The uncertainties were calculated using a bootstrap procedure (Helminiak et al. 2012), which is sensitive to the S/N of a component and velocity of rotation. The RVs were estimated as 40.20 ± 0.57 km s⁻¹ and 34.66 ± 0.85 km s⁻¹ for the spectra observed at the first and second epochs, respectively. We also checked for the consistency of RV measurements using broadening functions (BFs; Rucinski 1999). The RVs were calculated using a rotational broadening model described in Moharana et al. (2023). The BF-RVs were consistent with the TODCOR-RVs within the errors. The final RVs were taken from TODCOR due to their high precision.

⁶ <https://www.nist.gov/pml/atomic-spectra-database>

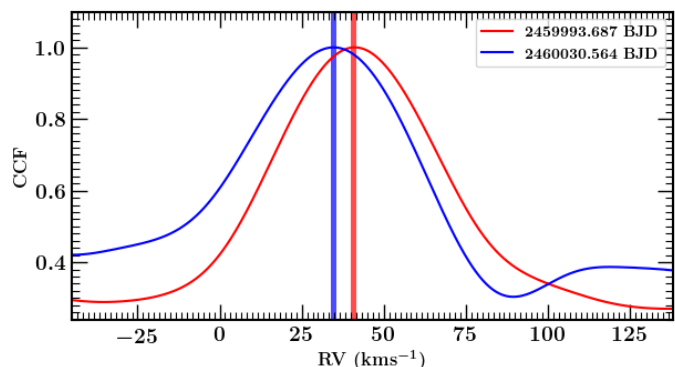


Fig. C.1. 1D projections of the TODCOR cross-correlation functions (CCFs) for the spectra observed at two epochs. The vertical shaded regions represent the errors in the observation of the RVs. The first epoch (red) has a RV of $40.20 \pm 0.57 \text{ km s}^{-1}$ and the second epoch (blue) has a RV of $34.66 \pm 0.85 \text{ km s}^{-1}$.

Appendix D: Simulation of binary configurations

To check the possible binary configurations of the identified PAGB star, we made a grid of models constrained by the observed radial velocities. We used the binary modelling code PHOEBE2 (Conroy et al. 2020 and references therein). Since we had two epochs of RV observations only, we considered the following assumptions for a simplified modelling:

1. The binary is edge-on. The inclination of the orbital plane is fixed at 87 degrees, and the orbital period is constrained to be less than 1000 days. For a wider orbit, we expect a high renormalised unit weight error (RUWE) parameter in Gaia DR3; however, the RUWE value of the PAGB star is 1.022 (< 1.4).
2. Models with orbits smaller than the radius of the PAGB star ($4.61 R_{\odot}$) or reaching the Roche limit will be rejected. We assume the secondary radius to be $1.00 R_{\odot}$.
3. The centre of mass (COM) or the gamma velocity of the binary is fixed at 12.6 km/s (the cluster mean).

The model generation followed these steps:

1. Setting up an initial model with random draws from a set of masses ($M_{\text{pri}} = 0.2, 0.5, 0.6, \text{ and } 0.8 M_{\odot}$), eccentricities ($e = 0.0, 0.2, 0.5, \text{ and } 0.8$), mass ratios ($q = 0.5, 1.0, \text{ and } 1.5$), and binary periods (P ; randomly between 0–90 days). The mass ratios and binary periods are guess values that are needed in order to initialise the PHOEBE2 set-up. We generated an initial set-up of 480 models.
2. We apply the constraints and then q , P , and time of periastron passage (T_p) to best fit the observed RV values. The optimisation was done using the Nelder-Mead method (Nelder & Mead 1965) for 500 iterations.
3. The optimisation discarded a few models if they failed to adhere to any pre-defined constraints. This gave us the final 396 models with possible q and P values.

The possible q and P values for our final binary models are shown in the left panel of Fig. D.1. The best-fit binary periods are clustered around three values: 39.12 ± 4.65 days (51.26 % of the models), 17.83 ± 1.26 days (16.4 %), and 6.65 ± 0.92 days (6.8%) (right panel of Fig. D.1). The mass ratio, q , varies between 0.2 and 1.5 (56 %; grey dashed

lines); however, the average values are around 1.0 for periods < 100 days (blue, red, orange, and green solid lines for masses 0.2, 0.5, 0.6, and $0.8 M_{\odot}$, respectively). We do not see any favourable eccentricity, but it is hard to constrain it with two epochs of observations.

In Fig. D.2 we provide the possible RV values for the primary (coloured solid lines) and companion stars (grey solid lines) for a period of 17.83 days (upper panels) and 39.12 days (lower panels). The maximum RV can reach $\sim 100 \text{ km/s}$ for the PAGB star with masses $0.6 M_{\odot}$ (period = 17.83 days) and $0.8 M_{\odot}$ (period = 39.12 days) (Fig. D.2).

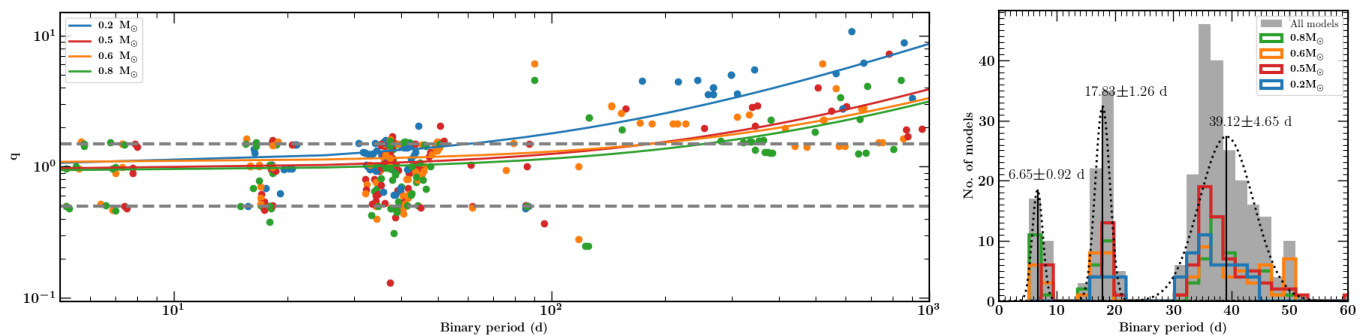


Fig. D.1. Orbital period and mass ratio values obtained from the best-fitting binary models. Left panel: Distribution of mass ratio (q) and orbital periods (P) with primary masses 0.2, 0.5, 0.6, and $0.8 M_{\odot}$ (blue, red, orange, and green dots, respectively). The solid lines are linear fits of the q and P values for the separate primary masses considered. The grey dashed lines denote the range of favourable q values for the system. 56.6 % of the models have mass ratios between 0.5 and 1.5. Right panel: Distribution of the period of the best-fit models. We see three significant period distributions at ~ 6 d, ~ 18 d, and ~ 39 d, with the 39 d distribution being more probable (51%).

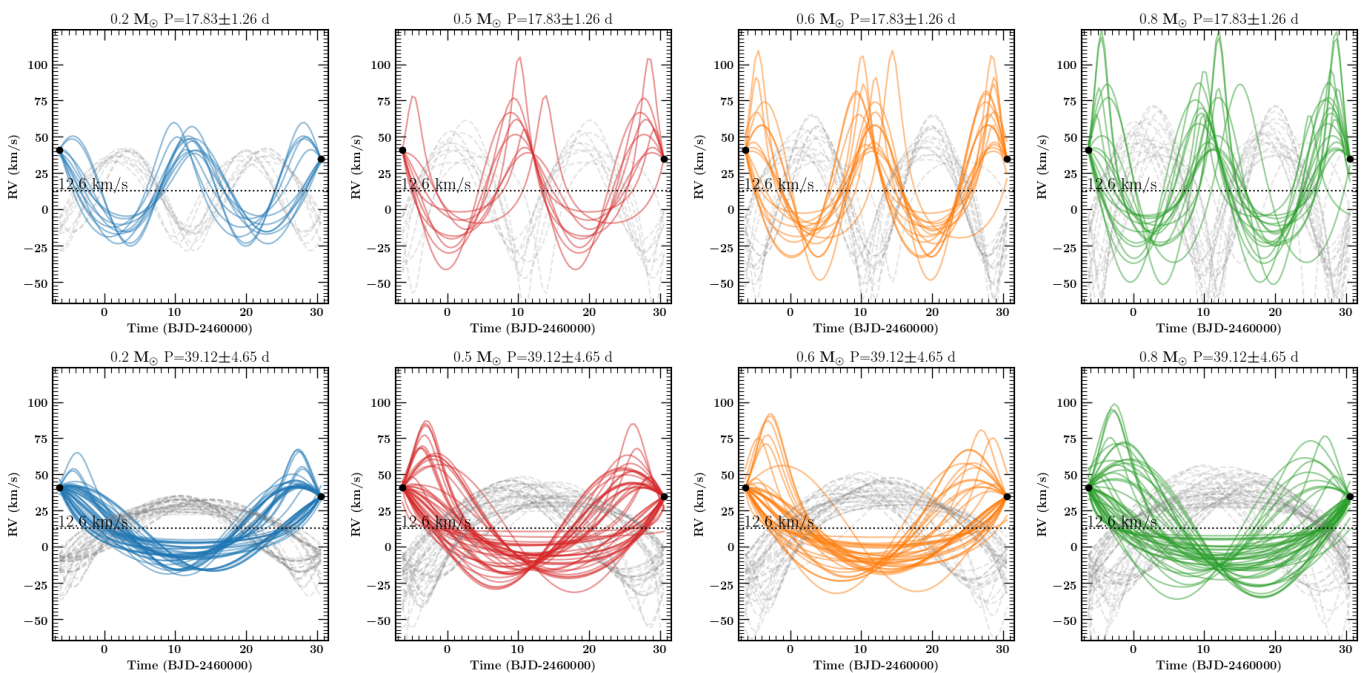


Fig. D.2. Possible Keplerian models for radial velocity variations constrained to the observations (black dots). The models are for PAGB mass $0.2 M_{\odot}$ (blue), $0.5 M_{\odot}$ (red), $0.6 M_{\odot}$ (orange), and $0.8 M_{\odot}$ (green) around the orbital periods 17.83 ± 1.26 days (upper panels) and 39.12 ± 4.65 days (lower panels). The dashed grey curves represent the possible RV of the secondary to maintain the COM velocity as 12.6 km/s (black dotted line).

Appendix E: Atmospheric parameter estimation from the high-resolution spectra

To derive the parameters of the stellar atmosphere from the CHIRON spectra, we used the TLUSTY model grid BSTAR2006 (Lanz & Hubeny 2007) and accompanied programs for calculating synthetic spectra (SYNSPEC, ROTIN; see Hubeny et al. 2021).

Synthetic profiles of the Balmer lines fit the observations only at a certain relation between T_{eff} and $\log g$. In the case of $H\alpha$ and $H\beta$ lines, these relations are similar in shape, but shifted relative to each other: $\log g_{\beta}(T_{\text{eff}}) = \log g_{\alpha}(T_{\text{eff}}) - 0.4$. The higher members of the Balmer series do not fall in the observed range (4505–6602 Å). Therefore, as the final relation for $\log g - T_{\text{eff}}$, we took the average between $H\alpha$ and $H\beta$ with an uncertainty of 0.2 dex.

The observations allowed us to construct a second relation involving the ionisation balance between Si II and Si III, whose lines are quite strong in the spectrum. We adjusted the silicon abundance (ϵ_{Si}) for each line of Si II $\lambda 6347$, 6371 and Si III $\lambda 4552$, 4567 , 4572 for a set of pairs (T_{eff} , $\log g$) along the found relation $\log g(T_{\text{eff}})$. For the true values of T_{eff} and $\log g$, the abundances ϵ_{Si} derived from Si II and Si III must coincide. We find that the coincidence of ϵ_{Si} over all lines Si III/Si II occurs at $T_{\text{eff}} = 16950 \pm 100 \text{ K}$, $\log \epsilon_{\text{Si}} = 7.31 \pm 0.03$, and $\xi = 1.5 \pm 0.5 \text{ km s}^{-1}$ (see Fig. E.1). A big uncertainty of the corresponding value of $\log g = 2.37 \pm 0.20$ leads to an increase in the temperature uncertainty, making it asymmetric $T_{\text{eff}} = 17000^{+300}_{-600} \text{ K}$. All calculations were made with the BSTAR2006 models with scaled solar abundances $Z/Z_{\odot} = 1/2$ (BL models) and $\xi = 2 \text{ km s}^{-1}$. We also redid all the calculations with the $Z/Z_{\odot} = 1/5$ (BS mod-

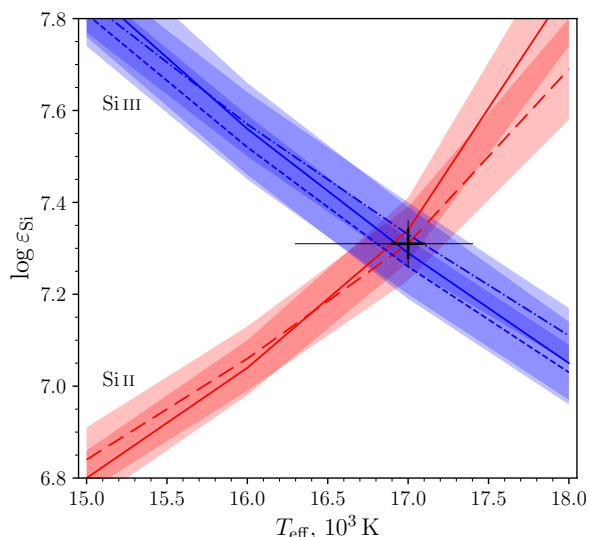


Fig. E.1. Silicon ionisation balance. Red is for Si II; the solid line is for Si II λ 6347, the dashed line is for Si II λ 6371. Blue is for Si III; the solid, dashed, dash-dotted lines are for Si III λ 4552, 4567, 4572, respectively. The shaded regions show the estimated uncertainties for each line.

els) and $\xi = 2 \text{ km s}^{-1}$ to know the effect of variations in the chemical composition in the models. We find that it does not affect the relation $\log g - T_{\text{eff}}$, but it reduces T_{eff} by 300 K in the diagram $T_{\text{eff}} - \log \varepsilon_{\text{Si}}$ and increases $\log \varepsilon_{\text{Si}}$ by 0.04 dex. Thus, the final results are $T_{\text{eff}} = 17000^{+400}_{-700}$ K, $\log g = 2.37 \pm 0.20$, and $\log \varepsilon_{\text{Si}} = 7.31 \pm 0.05$.

Appendix F: Chemical composition of the individual elements

Table F.1. Element abundances determined for the identified PAGB star. The abundances are estimated as $\log \varepsilon = 12 + \log(n_{\text{X}}/n_{\text{H}})$ and $[X/H] = \log(n_{\text{X}}/n_{\text{H}}) - \log(n_{\text{X}\odot}/n_{\text{H}\odot})$. The solar values $\log \varepsilon_{\odot}$ are from Asplund et al. (2009); σ_L is the standard deviation; $\bar{\sigma}$ is the final uncertainty, accounting for inaccuracies in the model parameters; N is the number of averaged lines.

	$\log \varepsilon_{\odot}$	$\log \varepsilon$	$[X/H]$	σ_L	$\bar{\sigma}$	N
He	10.93	11.00	+0.07	0.03	0.08	4
C	8.43	7.70	-0.73	0.03	0.07	2
N	7.83	7.56	-0.27	0.29	0.3	9
O	8.69	8.43	-0.26	0.04	0.07	4
Ne	7.84	7.57	-0.27	0.02	0.03	3
Al	6.45	5.61	-0.84	0.18	0.19	2
Si	7.51	7.31	-0.20	0.03	0.05	5
S	7.12	< 6.59	< -0.53	-	-	6
Fe	7.50	6.80	-0.70	-	0.2	1

Helium. He I λ 4713, 4922, 5016, 5048, 5876 lines are considered. We removed the He I λ 4922 line from the averaging, because it is blended with some broad absorption feature and shows $\log \varepsilon_{\text{He}}$ lower by 0.2 dex in comparison with the other lines. The rest of the lines agree well with

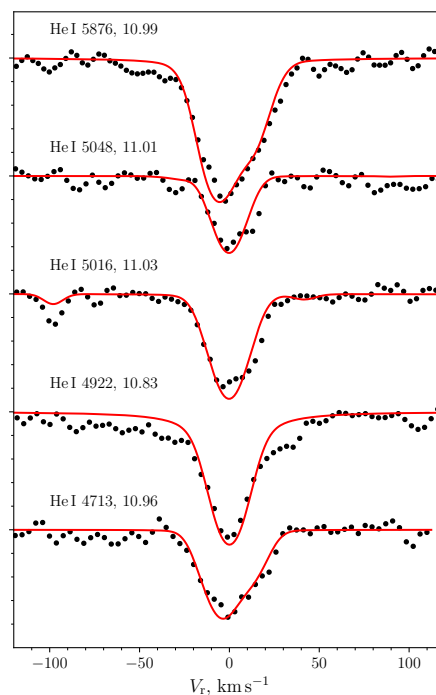


Fig. F.1. Observed profiles of He I lines (dots) are superposed on the model spectra (red lines). The numbers represent the values of $\log \varepsilon_{\text{He}}$.

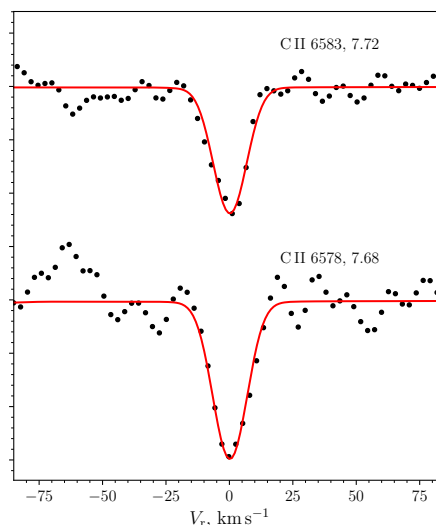


Fig. F.2. C II line profiles. The plot symbols are the same as in Fig. F.1. The numbers represent the values of $\log \varepsilon_{\text{C}}$.

each other. Figure F.1 shows the He I line profiles and fragments of the synthetic spectrum.

Carbon. The abundance ε_{C} is derived from two strong lines C II λ 6578, 6583. Figure F.2 shows the C II lines profiles superposed on model spectra.

Nitrogen. The observed spectrum contains several weak lines: N II λ 4601, 4607, 4630, 5000, 5001, 5005, 5011, 5667, 5680. The abundances derived from the various lines do not agree well with each other; stronger lines require a higher abundance than weaker ones. It indicates a high microturbulence.

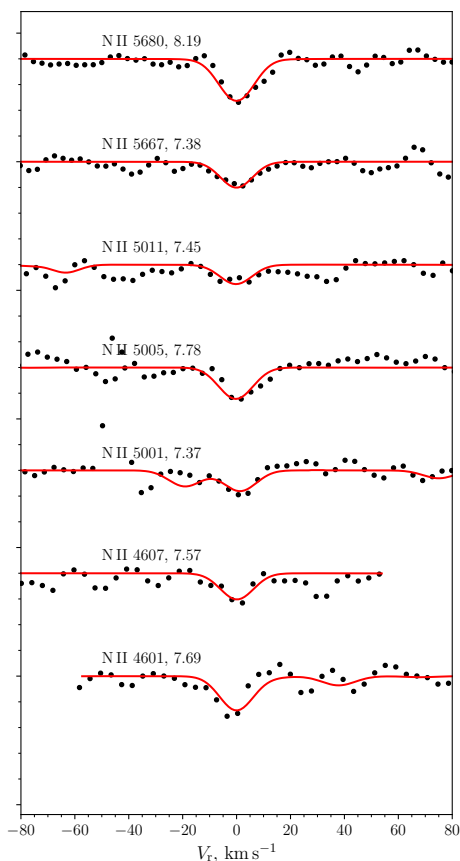


Fig. F.3. N II line profiles. The plot symbols are the same as in Fig. F.1. The numbers represent the values of $\log \epsilon_{\text{N}}$.

bulence velocity $\xi > 10 \text{ km s}^{-1}$, but the observed width of the lines is small and almost completely determined by the instrumental profile that puts a limit on $\xi < 5 \text{ km s}^{-1}$. Figure F.3 shows the N II line profiles superposed on model spectra.

Oxygen. A few weak lines of O II are seen in the spectrum. We used O II $\lambda\lambda 4642, 4649, 4662,$ and 4676 . Figure F.4 shows the O II lines profiles superposed on model spectra.

Neon. The abundance ϵ_{Ne} is derived from Ne I $\lambda\lambda 6143, 6402,$ and 6507 , which agree well with each other. There are two weaker lines Ne I $\lambda\lambda 6266, 6599$, but they show a $\log \epsilon_{\text{Ne}}$ value that is 0.3 dex lower and 0.3 dex higher than the rest of the lines.

Aluminium. Two lines are used: Al III $\lambda\lambda 5697, 5723$.

Silicon. The silicon abundance is determined simultaneously with the atmospheric parameters (see above).

Sulphur. We considered lines S II $\lambda\lambda 5014, 5032, 5432, 5454, 5640,$ and 5647 , although only the lines $\lambda\lambda 5014, 5640,$ and 5647 are reliably present in the observed spectrum. These lines give $\log \epsilon_{\text{S}} = 6.51, 6.26,$ and 6.59 , respectively. The S II $\lambda 5032$ line is relatively weak, but it is in agreement with the above-mentioned ϵ_{S} . However, at this abundance the lines S II $\lambda\lambda 5432, 5454$ must be present in the observations. The absence of these lines puts a limit $\log \epsilon_{\text{S}} \lesssim 5.5$. In any case, there is a sulphur deficiency $\log \epsilon_{\text{S}} < 6.59$ ($[\text{S}/\text{H}] < -0.53$).

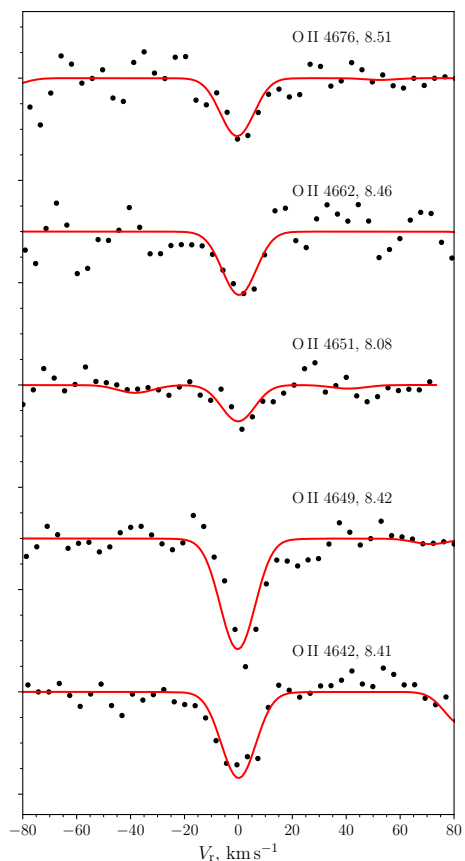


Fig. F.4. O II line profiles. The plot symbols are the same as in Fig. F.1. The numbers represent the values of $\log \epsilon_{\text{O}}$.

Iron. Only one Fe line Fe III $\lambda 5156$ is visible in the spectrum and gives $\log \epsilon_{\text{Fe}} = 6.8$. More weaker lines Fe II $\lambda\lambda 5018, 5169$ and Fe III $\lambda 5127$ are predicted by the model and agree with the observations within the uncertainties at the found abundance. The Fe lines are very weak in the spectra of early-type stars, making the estimate of metallicity based on iron a very difficult task. Therefore, we must rely on the CNO abundances as metallicity proxies (Mello et al. 2012). For the star, we found that $Z(\text{CNO})$ is equal to 0.005, compared to the solar value of 0.012.

The final uncertainty $\bar{\sigma}$ we estimated as $\bar{\sigma}^2 = \sigma_L^2 + \sigma_T^2 + \sigma_g^2 + \sigma_\xi^2 + \sigma_M^2$, where $\sigma_T, \sigma_g,$ and σ_ξ are uncertainties in $\log \epsilon,$ related to the uncertainties of $T_{\text{eff}}, \log g,$ and $\xi,$ respectively. The quantity σ_M is an estimate of the uncertainty associated with the difference between the real metallicity and the given metallicity of the BL models.

Appendix G: SED fitting of the PAGB star

The SED fitting of the PAGB star was performed using 30 photometric fluxes observed in different filters ranging from the UV to IR bands (Table G.1) and the theoretical fluxes from the TLUSTY non-LTE O/B stellar atmosphere model⁷ (TLUSTY model; Hubeny & Lanz 1995; Lanz & Hubeny 2007; Hubeny et al. 2021). The SED fitting proce-

⁷ <http://tlusty.oca.eu/Tlusty2002/tlusty-frames-cloudy.html>

Table G.1. Telescopes and their filters used in the SED fittings of the UVIT observed PAGB star.

Telescope/Survey	Filters	Wavelength range	Reference
UVIT	BaF2, Sapphire	1350–1800 Å	This paper
<i>GALEX</i>	FUV, NUV	1350–3000 Å	Schiavon et al. (2012)
Swift/UVOT	UVW2, UVM2, UVW1	1600–4700 Å	HEASARC Archive
Gaia	G, BP, RP	3300–10600 Å	Vasiliev & Baumgardt (2021)
CTIO-4m	U, B, V, R, I	3000–11800 Å	Stetson et al. (2019)
APASS	B, V, g, r, i	4300–7457 Å	Henden et al. (2015)
DENIS	I, J, Ks	7861–21453 Å	Denis (2005)
2MASS	J, H, Ks	12000–21500 Å	Skrutskie et al. (2006)
WISE	W1, W2, W3, W4	34000–220000 Å	Cutri et al. (2021)

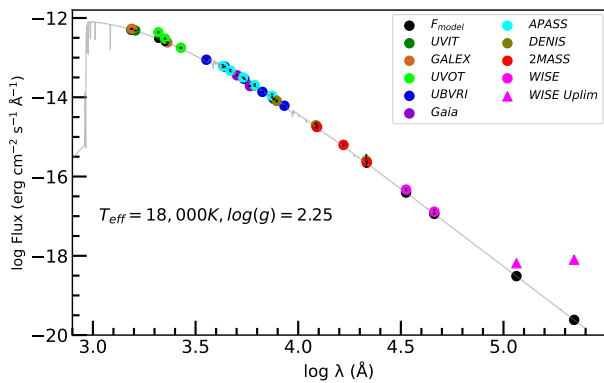


Fig. G.1. SED fit of observed fluxes in UVIT, GALEX, UVOT, UVBRI, Gaia DR3, APASS, DENIS, 2MASS, and WISE filters (30 photometric fluxes in total from UV to IR) for the PAGB star. The coloured solids are the observed fluxes, the black solids are the best-fitting model fluxes, and the grey solid is the best-fitting TLUSTY model grid spectra.

ture was performed in VO SED Analyzer⁸ (VOSA; Bayo et al. 2008). We fitted the observed photometric fluxes with the TLUSTY model grids and found that the best-fitting model grid has $T_{\text{eff}}=18\,000$ K and $\log g = 2.25$. The best-fitting model and observed fluxes are shown in Fig. G.1.

⁸ <http://svo2.cab.inta-csic.es/theory/main/>